www.sciencemag.org/content/342/6164/1346/suppl/DC1

Supplementary Material for

Phosphorus in the Young Supernova Remnant Cassiopeia A

Bon-Chul Koo,* Yong-Hyun Lee, Dae-Sik Moon, Sung-Chul Yoon, John C. Raymond

*Corresponding author. E-mail: koo@astro.snu.ac.kr

Published 13 December 2013, *Science* **342**, 1346 (2013)
DOI: 10.1126/science.1243823

This PDF file includes:

Supplementary Materials

S1. Observation and data reduction

The near-infrared (NIR) spectroscopic observations of Cassiopeia A (Cas A) were carried out with the TripleSpec spectrograph mounted on the 5-m Palomar Hale telescope on June 29 and August 8, 2008. TripleSpec is a slit-based NIR cross-dispersion echelle spectrograph covering the entire NIR atmospheric windows simultaneously with a spectral resolving power $R \approx 2500$–3000 (*29, 30*). The slit width and length of TripleSpec are $1''$ and $30''$, respectively. We obtained spectra at eight slit positions well spread over the bright, main shell of Cas A (see Fig. 1 in the Report). At each position, reference background spectra were obtained either within the slit, by observing the target at the two nod positions at $1/3$ (A) and $2/3$ (B) locations along the slit in an ABBA pattern, e.g., see (*31*), or outside the slit if the field was too crowded to obtain useful background spectra within the slit. The background spectra were then subtracted out. In Fig. 1, the positions represented by long ($45''$) white bars are where the spectra were obtained in the ABBA pattern, while the positions represented by the $30''$-long white bars are where the reference spectra were obtained outside the slit. The total exposure time per slit ranged from 300 sec to 1,800 sec.

For the data reduction, we followed the standard procedure of pre-processing including dark subtraction, flat-fielding correction, and bad pixel removal. We then obtained wavelength solutions using the OH airglow emission lines in the band, and corrected the wavelength to the heliocentric reference frame. The sky background including OH lines were subtracted out as much as possible

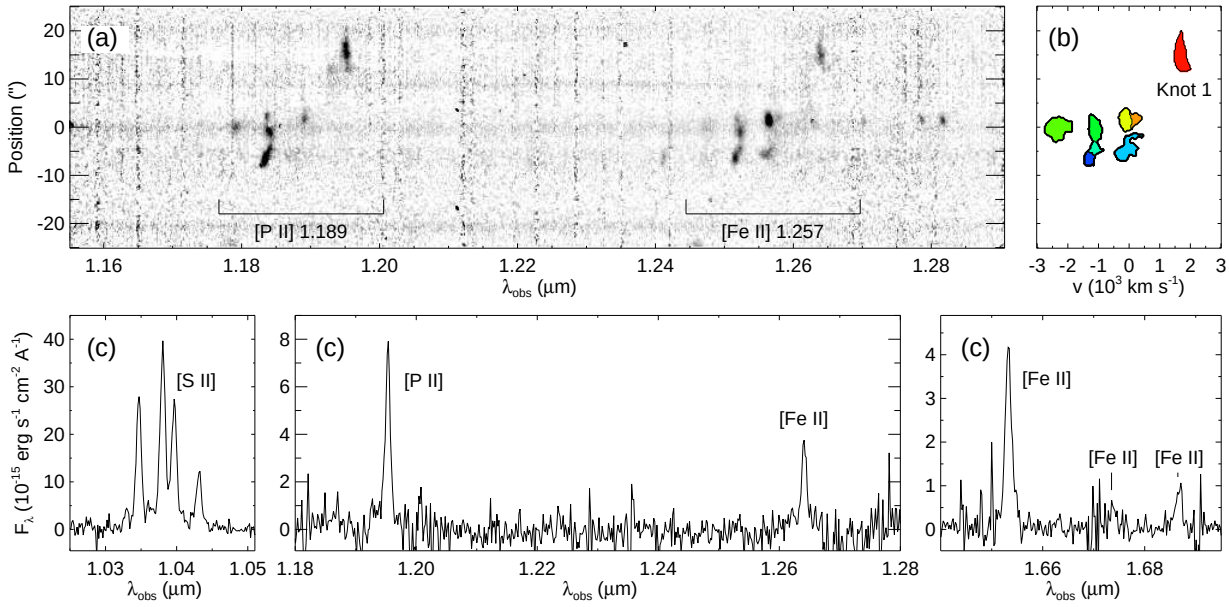

Figure S1: (a) Portion of the two-dimensional dispersed image of Slit 1 showing [P II] 1.189 μm and [Fe II] 1.257 μm lines. (b) Color-coded 'mask image' showing the areas in the two-dimensional dispersed image occupied by individual knots identified from the *Clumpfind* routine (*32*). The abscissa is the radial velocity determined from the Doppler shifts of the lines. (c) One dimensional spectrum of Knot 1 extracted from (a) using the mask in (b).

using the dithered or background frames. The flux calibration was done by comparing the spectra of the nearby A0V standard star (HD 223386) observed just before or after the target observations to the Kuruz model spectrum. We estimate a systematic uncertainty of 30% in the absolute flux, but this uncertainty did not enter into the analysis of relative abundances.

Along a slit, there are usually several [Fe II]-line emitting filaments or knots of distinct kinetic properties, so that, in a two-dimensional dispersed image, we observe complex emission

features distributed along both the space and velocity (or wavelength) dimensions. For example, Fig. S1 (a) shows a portion of the processed dispersed image of Slit 1, where we see more than five distinct "knots" emitting both [P II] 1.189 and [Fe II] 1.257 μm lines. In order to study the physical conditions of the emitting regions, we first need to separate out individual emission features. We used the clump-finding algorithm *Clumpfind* (*32*), which is developed for the identification of clumps in molecular clouds. Using a set of contour levels provided as an input parameter, the routine searches local maxima, decomposes clumps, and determines their locations and sizes. We used a set of contour levels starting at 2σ of the background RMS noise with a 2σ increment. The identification has been made in the dispersed image of the [Fe II] 1.644 μm line which is essentially identical to that of the [Fe II] 1.257 μm line in Fig. S1(a). If the [Fe II] line is weaker than the [S III] 0.953 μm or [P II] 1.189 μm lines, we used the latter. Fig. S1 (b) shows the result of applying *Clumpfind* to Slit 1, which yielded eight knots in total. These "masks" in dispersed images are then used to extract one-dimensional spectra of the knots. Fig. S1 (c) shows the extracted one-dimensional spectrum of Knot 1. The line fluxes are derived from Gaussian least-squares fittings of the spectra.

The derived line parameters of the five emission lines used in our analysis are listed in Table S1. The radial velocities are those of [Fe II] 1.257 μm lines, which agree with those of the other lines within about 100 km s^{-1}, comparable with the spectral resolution of our data. Note that the line fluxes are extinction corrected based on the ratio of [Fe II] 1.257 and 1.644 μm lines. Since these two lines share the same upper level ($a^4D_{7/2}$) (see the next section), their line ratio is determined by the ratio of $A_{21}\nu_{21}$ where A_{21} is Einstein A coefficients for spontaneous transition

from the upper (2) to the lower (1) state and ν_{21} is the frequency of the line. We adopt the recent theoretical result of (*33*), which gives the intrinsic ratio $F_{1.257}/F_{1.644} = 1.36$. The deviation of the observed line ratio from this is due to the extinction, and the corresponding corrections are applied to the other lines using the extinction curve of the carbonaceous-silicate grain model with Milky Way size distribution for $R_V = 3.1$ (*34*).

We note that there is a weak [Fe II] line at 1.18848 μm ($a^2G_{7/2} \rightarrow a^4D_{7/2}$) that overlaps with [P II] 1.189 (1.18861) μm line. Its expected intensity relative to the [Fe II] 1.257 μm line is $\lesssim 10^{-5}$ at the electron densities $\lesssim 10^5$ cm^{-3}, and consequently its contribution to the [P II] line flux should be negligible. The identification of this line reported in previous studies (*11, 35*) is most likely a misidentification of the [P II] line.

S2. Abundance analysis of [P II] and [Fe II] emission lines

In this section, we describe the basic properties of the forbidden lines that we use in our analysis and how we analyze them to derive the abundance ratios.

Near-infrared forbidden lines of P^+ and Fe^+

The lines that we use in our analysis are the forbidden lines from P II and Fe II. The energy level diagrams of the ground terms of these ions are shown in Fig. S2. P II is a p^2-ion and has three low-lying terms. The ground term (^3P) is split into three fine-structure levels, and the transition from $^1D_2$ to these levels produces three lines in the NIR band. Their wavelengths are

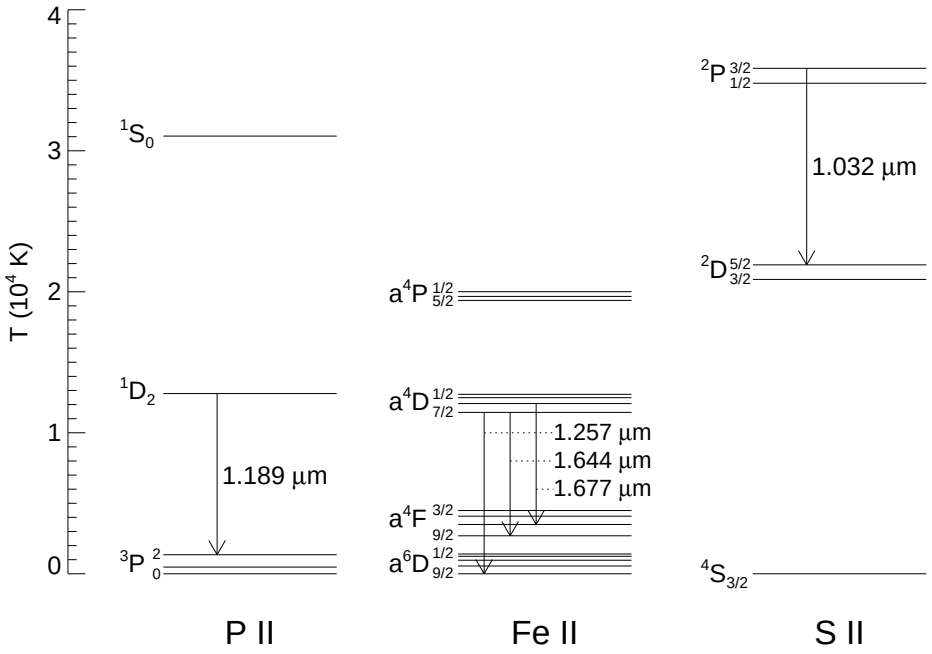

Figure S2: Energy-level diagrams for lowest terms of P II, Fe II, and S II in their ground electronic configurations. The emission lines used in this work are indicated by arrows with their wavelengths (in μm) labeled. The energies of upper terms are indicated on the left in temperature scale. The separations of the fine structure levels are magnified for clarity.

1.18861, 1.14713, and 1.12583 μm, and, using the Einstein coefficients in Table S2, their intensity ratios are $1 : 0.380 : 1.37 \times 10^{-4}$. We use the dominant 1.18861 μm line in our analysis. Fe II has four ground terms, each of which has closely-spaced 3–5 levels to form a 16 level system. The transitions among these levels produce many lines that appear in the near- to mid-infrared bands (*36, 37*). The lines to be analyzed in this work are the 1.25702, 1.64400, and 1.67734 μm lines. The first two lines are the two strongest [Fe II] lines, and as we pointed out in section S1, their intrinsic ratio is constant (=1.36).

In Fig. S2, we also show the energy level diagram of S II for completeness. The transitions among the fine structure levels $^2P_{3/2,1/2}$ and $^2D_{5/2,3/2}$ produce four adjacent forbidden lines, the strongest of which is the 1.032 μm line (see Fig. S1). Note that the excitation energy of the [S II] 1.032 μm line is significantly higher than those of [P II] and [Fe II] lines, which makes the ratio of [S II] 1.032 μm line to the other lines sensitive to T_e. In contrast, the excitation energies of the upper states of [P II] 1.189 and [Fe II] 1.257 μm lines are comparable to each other (Table S2), and we can derive a reliable abundance ratio using these two lines.

Formulation of abundance analysis

The general expression for the flux (erg cm^{-2} s^{-1}) of an optically thin, ionic spectral line from a knot is given by the integration of surface brightness (I_{21}) over the solid angle of the source:

$$F_{21} = \int I_{21} d\Omega = \frac{h\nu_{21}}{4\pi d^2} N_2 A_{21} = \frac{h\nu_{21}}{4\pi d^2} A_{21} f_2 f_{\rm ion} N_Z \quad (1)$$

where N_2 is the number of ions in the upper state, N_Z the total number of element Z, $f_{\rm ion} (\equiv N_{\rm ion}/N_{\rm Z})$ the fractional ionization of the element, $f_2 (\equiv N_2/N_{\rm ion})$ the fractional population of the upper level, and d the distance to the source. This, together with the line parameters in Table S2, gives the flux ratio of the [P II] 1.189 μm line to the [Fe II] 1.257 μm line

$$\frac{F_{\rm [PII]1.189}}{F_{\rm [FeII]1.257}} = 2.87 \frac{f_{\rm ^1D_2,PII}}{f_{\rm a^4D_{7/2},FeII}} \frac{f_{\rm PII}}{f_{\rm FeII}} X({\rm P/Fe}), \quad (2)$$

where $X({\rm P/Fe}) \equiv N_{\rm P}/N_{\rm Fe}$ is the abundance ratio that we intend to obtain.

The fractional population of the upper level (f_2) can be calculated for given n_e and T_e by solving rate equations. When the density is low, collisional excitation and de-excitation are negli-

gible compared to spontaneous radiative transition, and vice versa. For level i, the critical density can be defined by (*38*)

$$n_{\rm cr} \equiv \Sigma A_{ji}(j<i)/\Sigma C_{ij}(j\neq i) \tag{3}$$

where ΣC_{ij} is the collisional (de-)excitation coefficient averaged over a Maxwellian-velocity distribution at temperature T_e. In terms of the dimensionless collision strength Ω_{21}, the excitation and de-excitation coefficients are given by

$$C_{12} = \frac{g_2}{g_1} C_{21} e^{-E_{12}/kT_e},\ \ C_{21} = 8.629\times10^{-8}\frac{\Omega_{21}}{g_2}\left(\frac{T_e}{10^4\ {\rm K}}\right)^{-1/2}. \tag{4}$$

Ω_{21} weakly depends on temperature. For Maxwellian-averaged collision strengths for electron-impact excitation, we use the results of (*39*) and (*40*) for [P II] and [Fe II] lines, respectively. The critical densities of [P II] and [Fe II] lines are 3–5×10^4 cm^{-3} at $T_e = 10,000$ K (Table S2).

The fractional ionization cannot be estimated easily. In collisional ionization equilibrium, the P II and Fe II fractions peak near unity at 16,000 and 13,000 K, respectively. The ionization fraction curves are similar with a slight shift in temperature. In shocked gas, however, the ionization curves are affected by time-dependent ionization and photoionization, so that the fractional ionization could be far from the equilibrium value. In the next section, we discuss the structure of shocked SN ejecta, and develop a simple model for the abundance analysis.

[P II] and [Fe II] emission from shocked SN ejecta

The physical structure of shocked SN ejecta has been discussed in several previous studies (*41–46*). A noticeable characteristic of the shocks propagating into SN ejecta composed of

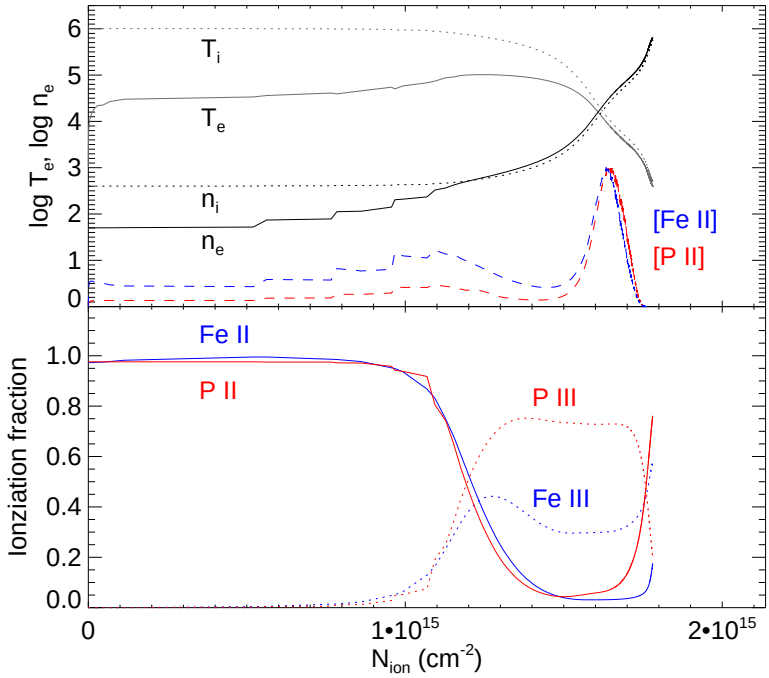

Figure S3: (top) Temperature and density profiles of electrons and ions as a function of swept-up ion-nuclei column density for a 50 km s^{-1} shock propagating into an oxygen-enriched SN ejecta of $n_{\rm ion} = 100$ cm^{-3}. [P II] 1.189 μm and [Fe II] 1.257 μm line emissivities per ion (erg s^{-1} sr^{-1}) are overplotted in a linear scale. (bottom) Ionization fraction profiles of phosphorus and iron. The calculation is done by using a shock code developed for SN ejecta (*45*, *47*, *48*) with updated atomic constants for phosphorus.

heavy elements is the strong cooling that occurs before the ions achieve equilibrium ionization states. This is shown in Fig. S3, where we plot the temperature and density profiles (top frame) and ionization fraction profiles of phosphorus and iron (bottom frame) of a 'typical' dense SN ejecta knot swept up by a reverse shock. Note that there is an extended "temperature plateau" region where electrons are at temperatures much lower than those of the ions. For the electron gas

in this region, the heating by Coulomb collisions with ions balances with the cooling by the collisional excitation and ionization of the ions. As the electron density increases, the cooling becomes efficient and the electron and ion temperatures drop, which happens in a very narrow region. In the plateau region, both phosphorus and iron atoms are mostly in singly ionized states, ionized by the Galactic background radiation field, i.e., $f_{\rm PII} \approx f_{\rm FeII} \approx 1$. In the cooling region, these fractions decrease as the ions become more highly ionized by electron collisions.

The [P II] and [Fe II] emission lines originate from both the temperature plateau and the cooling regions. The cooling region is very thin and the fractions of the singly ionized ions are low, but these are compensated by the increase in electron density, so that, depending on shock speed, preshock density, and chemical composition, the emission from the cooling region can dominate. In principle, there could be some emission from the preshock region photoionized by the shock radiation (*43*,*44*,*46*), but in the Cas A knots the observed high electron densities (3×10^3–2×10^5 cm^{-3}; see below) indicate that the observed [P II] and [Fe II] emission lines are mostly from the shocked gas.

In SN ejecta swept-up by a reverse shock, it is likely that a wide range of preshock densities and also a wide range of shock speeds are present (*44*,*45*). We ran a grid of models and have found that, in order to match the observed [Fe II] line ratios, the shock speed should be $\lesssim 50$ km s^{-1} and the preshock densities should be $\gtrsim 100$ cm^{-3}. For such slow shocks in dense SN ejecta, a simple model where the emitting region is at $T_e = 10,000$ K and has an uniform density (determined from the [Fe II] line ratios) with $f_{\rm PII}/f_{\rm FeII} = 1$ yields P/Fe abundance ratio accurate to within

about 30%. For example, the assumed $X(\mathrm{P/Fe})$ in the model used in Fig. S3 was 0.10 while it is 0.090 if we apply the simple model to the resulting [Fe II] 1.667/[Fe II] 1.644 and [P II] 1.189/[Fe II] 1.257 [Fe II] line ratios. This is because firstly the upper states of the [P II] 1.189 μm and [Fe II] 1.257 μm lines have comparable excitation energies (12,780 and 11,450 K), so that the level-population ratio ($f_{^1\mathrm{D}_2,\mathrm{PII}}/f_{\mathrm{a}^4\mathrm{D}_{7/2},\mathrm{FeII}}$) is almost independent of temperature and is mainly a function of electron density n_e. Secondly their critical densities are comparable (3–5$\times10^4$ cm^{-3}) and P and Fe have comparable ionization energies, i.e., 10.49 vs. 7.90 eV for I$\rightarrow$II and 19.77 vs. 16.19 eV for II$\rightarrow$III, so that the two lines are emitted from nearly the same spatial volume as we see in Fig. S3. Therefore, we can obtain a reliable estimate of the abundance ratio $X(\mathrm{P/Fe})$ from a simple model. Note that this simple model is also applicable for the circumstellar knots of normal chemical composition where the emission is from dense, cooling regions.

Fig. S4 (top) shows the [P II] and [Fe II] line ratio as a function of electron density at $T_e = 10,000$ K. We also show the curves for $T_e = 5,000$ and 20,000 K for comparison. The temperature dependence is weak as expected. A great advantage of the broadband NIR spectroscopy is that there exist many [Fe II] lines that can be used to derive electron density. One such set is [Fe II] 1.644 and 1.677 μm lines. Fig. S4 (bottom) shows that the intensity ratio of the two lines is almost independent of temperature. Hence, for a given knot, we can first derive the electron density from $F_{[\mathrm{FeII}]1.677}/F_{[\mathrm{FeII}]1.644}$, and use this density to estimate $X(\mathrm{P/Fe})$. The mean observed $F_{[\mathrm{FeII}]1.677}/F_{[\mathrm{FeII}]1.644}$ ratio is 0.167 ± 0.046, corresponding to $n_e = 2.1 \times 10^4$ cm^{-3}. However, the variations among the knots are large, and electron densities corresponding to $\pm2\sigma$ deviations from the mean (3.5×10^3–1.8×10^5 cm^{-3}) are marked by dotted lines in Fig. S4. It is worth noting that,

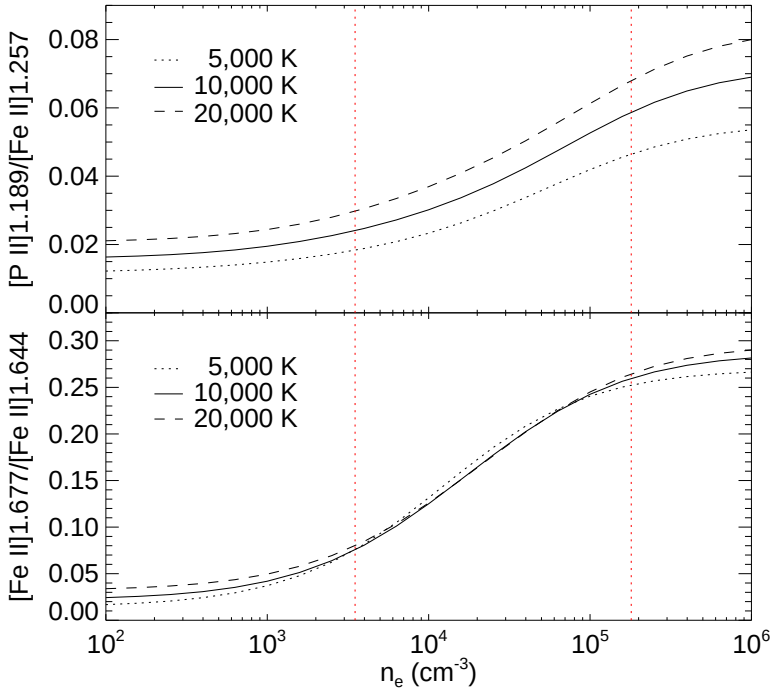

Figure S4: (top) [P II] 1.189/[Fe II] 1.257 line intensity ratio for different temperatures. Note that it assumes $f_{\rm PII} = f_{\rm FeII}$ and the solar abundance, i.e., $N({\rm P})/N({\rm Fe}) = 8.1 \times 10^{-3}$[1]. The range ($\pm 2\sigma$) of the electron densities of the Cas A knots are marked by dotted lines. (bottom) [Fe II] 1.677/[Fe II] 1.644 line intensity ratio as a function of n_e for different temperatures.

for the range of the electron densities of the Cas A knots, the flux ratio can be written as

$$\frac{F_{\rm [PII]1.189}}{F_{\rm [FeII]1.257}} = (3-7)X({\rm P/Fe}). \tag{5}$$

Table S1. **Flux table for the identified near-infrared knots.**

Slit	**Knot**	**l**	$\mathbf{v_{rad}}$	**d**	**F_λ [10^{-15} erg s^{-1} cm^{-2}]**					
No.	**No.**	[″]	[km/s]	[″]	[S II]$_{1.032}$	He I$_{1.082}$	[P II]$_{1.189}$	[Fe II]$_{1.257}$	[Fe II]$_{1.644}$	[Fe II]$_{1.677}$
1	1	8.75	1696	118.3	5541(32)	≤46	719(14)	312(13)	230(4)	55(3)
1	2	3.25	195	104.8	2226(53)	≤53	253(11)	136(8)	100(3)	8(2)
1	3	5.00	-81	104.6	≤32	1430(7)	≤13	290(3)	213(2)	38(2)
1	4	5.50	-2244	103.1	1054(6)	≤8	62(4)	23(3)	17(3)	≤2
1	5	5.75	-1100	101.8	1060(10)	≤9	174(5)	120(3)	88(1)	17(3)
1	6	3.00	-1113	98.3	352(4)	≤4	55(3)	32(2)	23(1)	6(2)
1	7	5.75	-87	97.3	≤164	≤79	≤36	406(15)	299(6)	15(4)
1	8	3.00	-1252	96.6	636(4)	≤5	129(3)	48(2)	35(1)	7(3)
2	1	4.50	136	95.9	≤30	≤27	≤12	70(5)	52(3)	4(1)
2	2	5.75	1176	95.6	1738(42)	≤41	117(24)	49(15)	36(5)	≤10
2	3	8.00	-702	97.6	1137(15)	≤13	197(8)	39(6)	29(3)	≤5
2	4	9.25	798	106.3	1294(26)	≤41	65(11)	216(9)	159(4)	22(2)
2	5	6.50	1122	106.3	1685(105)	≤61	120(23)	297(27)	218(8)	≤10
2	6	3.75	1337	108.4	983(43)	≤27	29(13)	106(16)	78(4)	5(2)
3	1	6.75	-485	107.8	2282(17)	93(15)	269(11)	252(6)	185(3)	33(2)

Table S1—Continued

Slit	**Knot**	**l**	**v_{rad}**	**d**	**F_λ [10^{-15} erg s^{-1} cm^{-2}]**					
No.	**No.**	[″]	[km/s]	[″]	[S II]$_{1.032}$	He I$_{1.082}$	[P II]$_{1.189}$	[Fe II]$_{1.257}$	[Fe II]$_{1.644}$	[Fe II]$_{1.677}$
3	2	5.00	-410	105.0	1259(11)	60(10)	116(7)	153(3)	113(2)	21(2)
3	3	7.25	-294	102.3	2960(10)	68(8)	273(8)	460(4)	339(2)	60(2)
3	4	6.50	194	99.6	794(13)	≤40	50(7)	199(5)	146(3)	24(1)
3	5	5.75	270	97.3	184(14)	≤24	≤8	47(5)	35(3)	5(1)
4	1	5.25	1002	95.3	≤396	≤144	≤76	447(56)	329(9)	≤7
4	2	3.75	1272	98.3	1145(41)	272(31)	≤20	240(13)	176(3)	21(2)
4	3	5.75	-513	100.0	≤26	57(10)	≤10	144(5)	106(2)	21(2)
4	4	6.25	859	101.5	5194(28)	≤37	304(14)	444(12)	327(3)	55(3)
4	5	4.00	-8	101.5	≤16	≤14	≤7	98(3)	72(2)	10(1)
4	6	5.75	393	102.0	1626(24)	≤42	134(13)	449(11)	330(4)	49(2)
5	1	5.25	1913	112.3	1465(68)	≤88	85(19)	302(21)	222(5)	33(4)
5	2	5.25	983	112.2	2658(51)	≤36	107(14)	338(14)	249(5)	58(3)
5	3	4.50	1350	112.1	≤91	≤25	≤20	171(13)	125(4)	10(2)
5	4A[a]	6.25	-118	112.2	3596(27)	≤217	94(15)	298(8)	220(3)	42(3)
5	4B[a]	6.25	-118	112.1	≤182	19435(68)	107(15)	1195(8)	880(3)	169(3)

Table S1—Continued

Slit No.	Knot No.	l [″]	v_{rad} [km/s]	d [″]	F_λ [10^{-15} erg s^{-1} cm^{-2}] [S II]$_{1.032}$	He I$_{1.082}$	[P II]$_{1.189}$	[Fe II]$_{1.257}$	[Fe II]$_{1.644}$	[Fe II]$_{1.677}$
5	5	5.25	1544	111.7	1188(31)	≤42	≤27	300(13)	220(3)	36(2)
5	6	4.75	-184	111.4	854(26)	≤120	≤28	165(11)	121(4)	25(3)
5	7	3.75	-494	111.3	536(18)	≤14	≤13	100(6)	73(2)	18(2)
5	8	5.00	605	110.8	1042(52)	≤76	136(22)	418(17)	308(6)	54(3)
5	9	1.75	1579	110.7	882(63)	≤52	≤33	101(16)	74(4)	7(3)
5	10	9.75	-293	110.8	≤98	422(37)	≤40	2564(11)	1887(4)	375(4)
6	1	3.50	1044	114.4	717(12)	≤19	17(6)	102(8)	75(3)	18(2)
6	2	3.25	1391	114.3	1150(21)	≤29	136(12)	215(13)	158(4)	21(2)
6	3	4.25	1913	114.5	833(23)	≤79	123(21)	514(13)	378(4)	61(3)
6	4A[a]	2.75	-159	114.1	≤111	470(25)	≤28	43(7)	32(4)	6(3)
6	4B[a]	2.75	-159	114.0	767(33)	≤55	107(22)	27(8)	20(4)	4(3)
6	5	3.00	1303	114.1	368(34)	≤17	≤16	130(9)	96(3)	15(3)
6	6	6.25	1540	113.7	2600(65)	159(25)	304(20)	565(20)	416(5)	69(3)
6	7	4.50	799	113.2	3858(23)	≤34	247(13)	318(9)	234(4)	48(2)
6	8	2.75	560	112.9	295(20)	≤27	≤35	113(7)	83(3)	13(2)

Table S1—Continued

Slit	Knot	l	v_{rad}	d	F_λ [10^{-15} erg s^{-1} cm^{-2}]					
No.	No.	[″]	[km/s]	[″]	[S II]$_{1.032}$	He I$_{1.082}$	[P II]$_{1.189}$	[Fe II]$_{1.257}$	[Fe II]$_{1.644}$	[Fe II]$_{1.677}$
6	9	2.75	528	112.8	≤41	≤23	≤26	143(7)	105(3)	18(2)
6	10	3.50	459	112.8	≤33	≤22	≤20	134(5)	99(2)	17(2)
6	11	6.50	-301	112.9	≤41	129(12)	≤22	295(6)	217(3)	34(2)
6	12	4.25	316	112.9	≤85	≤41	≤31	67(10)	50(4)	7(3)
7	1	3.25	1586	121.8	791(27)	≤34	97(11)	124(8)	91(2)	14(2)
7	2	5.50	-73	123.5	≤23	717(15)	18(6)	240(4)	176(3)	44(1)
7	3	4.00	35	128.5	≤20	731(19)	33(6)	372(3)	274(4)	55(1)
7	4	2.75	75	129.9	≤24	1125(20)	26(6)	276(4)	203(5)	40(1)
7	5	3.25	-78	131.2	≤39	4082(19)	31(9)	331(5)	244(4)	40(2)
8	1	3.25	703	121.9	3294(16)	105(16)	229(8)	96(7)	71(3)	10(2)
8	2	6.00	818	119.2	2161(23)	68(15)	215(9)	182(8)	134(4)	28(2)
8	3	6.25	715	114.9	2013(16)	51(12)	318(9)	210(7)	154(4)	24(2)
8	4	5.25	608	112.0	4789(24)	266(54)	595(11)	235(9)	173(3)	26(2)
8	5	4.50	613	109.4	4484(66)	≤60	567(24)	145(20)	107(6)	11(3)
8	6	4.00	473	108.6	12167(143)	≤140	855(44)	192(28)	141(6)	20(3)

Table S1—Continued

Slit	**Knot**	**l**	$\mathbf{v}_{\rm rad}$	**d**	$\mathbf{F_\lambda}$ **[10^{-15} erg s^{-1} cm^{-2}]**					
No.	**No.**	[″]	[km/s]	[″]	[S II]$_{1.032}$	He I$_{1.082}$	[P II]$_{1.189}$	[Fe II]$_{1.257}$	[Fe II]$_{1.644}$	[Fe II]$_{1.677}$
8	7	4.75	640	106.5	4108(67)	$\leq$45	681(18)	255(16)	188(5)	28(3)
8	8	4.00	122	106.4	331(15)	$\leq$47	113(8)	103(6)	76(4)	16(2)
8	9	4.00	359	105.0	461(19)	$\leq$31	210(11)	158(8)	117(3)	22(2)

Note. — Columns 1–5 present slit number, knot number, angular size along the slit (l), radial velocity ($v_{\rm rad}$), and distance (d) from the explosion center ($\alpha = 23^{\rm h}23^{\rm m}27^{\rm s}.77 \pm 0^{\rm s}.05$, $\delta = 58^\circ48'49''.4 \pm 0''.4$ [J2000])[28]. The slit number starts from the top and increases in a counterclockwise direction (Fig. 1 in Report). Note that Slits 5 and 6, represented by relatively short white bars, are located side by side with the former slightly inside. Columns 6–11 present extinction-corrected fluxes of [S II] 1.032, He I 1.082, [P II] 1.189, [Fe II] 1.257, [Fe II] 1.644, and [Fe II] 1.677 μm lines. The intensity ratio of the [Fe II] 1.257 and [Fe II] 1.644 μm lines is constant (1.36) because they share the same upper level (see text). The number in bracket denotes a 1σ error of each flux from the Gaussian fit, whereas the upper limits are 3σ limits.

[a]These knots in Slits 5 and 6 have been identified as a single knot by *Clumpfind* respectively, but a detailed inspection revealed that each of them are composed of two (A and B) components almost coincident both in space and velocity.

;

Table S2. **Parameters of near-infrared [P II] and [Fe II] lines used in the analysis.**

	transition levels		λ	A_{21}	$n_{\rm cr}$	$T_{\rm ex}$
ion	lower	upper	(μm)	(s^{-1})	(cm^{-3})	(K)
P II	$^3P_2$	$^1D_2$	1.18861	1.43×10^{-2}	5.3×10^4	12,780
	$^3P_1$	$^1D_2$	1.14713	5.24×10^{-3}	5.3×10^4	12,780
	$^3P_0$	$^1D_2$	1.12583	1.85×10^{-6}	5.3×10^4	12,780
Fe II	$a^6D_{9/2}$	$a^4D_{7/2}$	1.25702	5.27×10^{-3}	3.5×10^4	11,446
	$a^4F_{9/2}$	$a^4D_{7/2}$	1.64400	5.07×10^{-3}	3.5×10^4	11,446
	$a^4F_{7/2}$	$a^4D_{5/2}$	1.67734	2.11×10^{-3}	3.1×10^4	12,074

Note. — Columns present ion, lower and upper transition levels, wavelength of the lines (λ), Einstein A values, critical density ($n_{\rm cr}$) at $T_e = 10,000$ K (see eq. [3] in the text), and excitation energy ($T_{\rm ex}$) of the upper level. The Einstein A values are from (*49*) and (*33*) for [P II] and [Fe II], respectively.

References and Notes

1. M. Asplund, N. Grevesse, A. J. Sauval, P. Scott, The chemical composition of the Sun. *Annu. Rev. Astron. Astrophys.* **47**, 481–522 (2009). doi:10.1146/annurev.astro.46.060407.145222

2. V. Lebouteiller, Kuassivi, R. Ferlet. *Astron. Astrophys.* **443**, 509 (2005). doi:10.1051/0004-6361:20053448

3. E. Caffau, P. Bonifacio, R. Faraggiana, M. Steffen, The Galactic evolution of phosphorus. *Astron. Astrophys.* **532**, A98 (2011). doi:10.1051/0004-6361/201117313

4. S. E. Woosley, T. A. Weaver, The evolution and explosion of massive stars. II. Explosive hydrodynamics and nucleosynthesis. *Astrophys. J. Suppl. Ser.* **101**, 181 (1995). doi:10.1086/192237

5. Another type of stellar explosions (Type Ia supernovae) are also thought to contribute, but to a much lesser extent (*26*, *27*).

6. J. E. Reed, J. J. Hester, A. C. Fabian, P. F. Winkler, The three-dimensional structure of the Cassiopeia A supernova remnant. I. The spherical shell. *Astrophys. J.* **440**, 706 (1995). doi:10.1086/175308

7. R. A. Fesen, M. C. Hammell, J. Morse, R. A. Chevalier, K. J. Borkowski, M. A. Dopita, C. L. Gerardy, S. S. Lawrence, J. C. Raymond, S. van den Bergh, The expansion asymmetry and age of the Cassiopeia A supernova remnant. *Astrophys. J.* **645**, 283–292 (2006). doi:10.1086/504254

8. O. Krause, S. M. Birkmann, T. Usuda, T. Hattori, M. Goto, G. H. Rieke, K. A. Misselt, The Cassiopeia A supernova was of type IIb. *Science* **320**, 1195–1197 (2008). doi:10.1126/science.1155788

9. U. Hwang, J. M. Laming, A *Chandra* x-ray survey of ejecta in the Cassiopeia A supernova remnant. *Astrophys. J.* **746**, 130 (2012). doi:10.1088/0004-637X/746/2/130

10. P. A. Young, C. L. Fryer, A. Hungerford, D. Arnett, G. Rockefeller, F. X. Timmes, B. Voit, C. Meakin, K. A. Eriksen, Constraints on the progenitor of Cassiopeia A. *Astrophys. J.* **640**, 891–900 (2006). doi:10.1086/500108

11. C. L. Gerardy, R. A. Fesen, Near-infrared spectroscopy of the Cassiopeia A and Kepler supernova remnants. *Astron. J.* **121**, 2781–2791 (2001). doi:10.1086/320393

12. Materials and methods are available as supplementary materials on *Science* Online.

13. S. van den Bergh, Optical studies of Cassiopeia A. III. Spectra of the supernova remnant. *Astrophys. J.* **165**, 457 (1971). doi:10.1086/150913

14. J.-J. Lee, S. Park, J. P. Hughes, P. O. Slane, arXiv:1304.3973 (2013)

15. E. Oliva, A. Marconi, R. Maiolino, L. Testi, F. Mannucci, F. Ghinassi, J. Licandro, L. Origlia, C. Baffa, A. Checcucci, G. Comoretto, V. Gavryussev, S. Gennari, E. Giani, L. K. Hunt, F. Lisi, D. Lorenzetti, G. Marcucci, L. Miglietta, M. Sozzi, P. Stefanini, F. Vitali, NICS-TNG infrared spectroscopy of NGC 1068: The first extragalactic measurement of [P II] and a new tool to constrain the origin of [Fe II] line emission in galaxies. *Astron. Astrophys.* **369**, L5–L8 (2001). doi:10.1051/0004-6361:20010214

16. T. Rauscher, A. Heger, R. D. Hoffman, S. E. Woosley, Nucleosynthesis in massive stars with improved nuclear and stellar physics. *Astrophys. J.* **576**, 323–348 (2002). doi:10.1086/341728

17. K. Kifonidis, T. Plewa, H.-T. Janka, E. Müller, *Astron. Astrophys.* **408**, 621 (2003). doi:10.1051/0004-6361:20030863

18. T. DeLaney, L. Rudnick, M. D. Stage, J. D. Smith, K. Isensee, J. Rho, G. E. Allen, H. Gomez, T. Kozasa, W. T. Reach, J. E. Davis, J. C. Houck, The three-dimensional structure of Cassiopeia A. *Astrophys. J.* **725**, 2038–2058 (2010). doi:10.1088/0004-637X/725/2/2038

19. S. E. Woosley, R. G. Eastman, T. A. Weaver, P. A. Pinto, SN 1993J: A Type IIb supernova. *Astrophys. J.* **429**, 300 (1994). doi:10.1086/174319

20. C. Kobayashi, H. Umeda, K. Nomoto, N. Tominaga, T. Ohkubo, Galactic chemical evolution: Carbon through zinc. *Astrophys. J.* **653**, 1145–1171 (2006). doi:10.1086/508914

21. A. Chieffi, M. Limongi, Pre-supernova evolution of rotating solar metallicity stars in the mass range 13-120 $M_{\odot}$ and their explosive yields. *Astrophys. J.* **764**, 21 (2013). doi:10.1088/0004-637X/764/1/21

22. J. Rho, T. Kozasa, W. T. Reach, J. D. Smith, L. Rudnick, T. DeLaney, J. A. Ennis, H. Gomez, A. Tappe, Freshly formed dust in the Cassiopeia A supernova remnant as revealed by the *Spitzer Space Telescope*. *Astrophys. J.* **673**, 271–282 (2008). doi:10.1086/523835

23. B. Sibthorpe, P. A. R. Ade, J. J. Bock, E. L. Chapin, M. J. Devlin, S. Dicker, M. Griffin, J. O. Gundersen, M. Halpern, P. C. Hargrave, D. H. Hughes, W.-S. Jeong, H. Kaneda, J. Klein, B.-C. Koo, H.-G. Lee, G. Marsden, P. G. Martin, P. Mauskopf, D.-S. Moon, C. B. Netterfield, L. Olmi, E. Pascale, G. Patanchon, M. Rex, A. Roy, D. Scott, C. Semisch, M. D. P. Truch, C. Tucker, G. S. Tucker, M. P. Viero, D. V. Wiebe, *Akari* and blast observations of the Cassiopeia A supernova remnant and surrounding interstellar medium. *Astrophys. J.* **719**, 1553–1564 (2010). doi:10.1088/0004-637X/719/2/1553

24. M. J. Barlow, O. Krause, B. M. Swinyard, B. Sibthorpe, M.-A. Besel, R. Wesson, R. J. Ivison, L. Dunne, W. K. Gear, H. L. Gomez, P. C. Hargrave, T. Henning, S. J. Leeks, T. L. Lim, G. Olofsson, E. T. Polehampton, A *Herschel* PACS and SPIRE study of the dust content of the Cassiopeia A supernova remnant. *Astron. Astrophys.* **518**, L138 (2010). doi:10.1051/0004-6361/201014585

25. T. Nozawa, T. Kozasa, N. Tominaga, K. Maeda, H. Umeda, K. Nomoto, O. Krause, Formation and evolution of dust in type iib supernovae with application to the Cassiopeia A supernova remnant. *Astrophys. J.* **713**, 356–373 (2010). doi:10.1088/0004-637X/713/1/356

26. G. Cescutti, F. Matteucci, E. Caffau, P. François, Chemical evolution of the Milky Way: The origin of phosphorus. *Astron. Astrophys.* **540**, A33 (2012). doi:10.1051/0004-6361/201118188

27. C. West, A. Heger, Metallicity-dependent galactic isotopic decomposition for nucleosynthesis. *Astrophys. J.* **774**, 75 (2013). doi:10.1088/0004-637X/774/1/75

28. J. R. Thorstensen, R. A. Fesen, S. van den Bergh, The expansion center and dynamical age of the galactic supernova remnant Cassiopeia A. *Astron. J.* **122**, 297–307 (2001). doi:10.1086/321138

29. J. C. Wilson, C. P. Henderson, T. L. Herter, K. Matthews, M. F. Skrutskie, J. D. Adams, D.-S. Moon, R. Smith, N. Gautier, M. Ressler, B. T. Soifer, S. Lin, J. Howard, J. LaMarr, T. M. Stolberg, J. Zink, *SPIE* **5492**, 1295–1305 (2004). doi:10.1117/12.550925

30. T. L. Herter, C. P. Henderson, J. C. Wilson, *SPIE* **7014**, 30 (2008).

31. J. R. Houck, T. L. Roellig, J. Van Cleve, W. J. Forrest, T. L. Herter, C. R. Lawrence, K. Matthews, H. J. Reitsema, B. T. Soifer, D. M. Watson, D. Weedman, M. Huisjen, J. R. Troeltzsch, D. J. Barry, J. Bernard-Salas, C. Blacken, B. R. Brandl, V. Charmandaris, D. Devost, G. E. Gull, P. Hall, C. P. Henderson, S. J. U. Higdon, B. E. Pirger, J. Schoenwald, G. C. Sloan, K. I. Uchida, P. N. Appleton, L. Armus, M. J. Burgdorf, S. B. Fajardo-Acosta, C. J. Grillmair, J. G. Ingalls, P. W. Morris, H. I. Teplitz, *SPIE* **5487**, 62–76 (2004). doi:10.1117/12.550517

32. J. P. Williams, E. J. de Geus, L. Blitz, Determining structure in molecular clouds. *Astrophys. J.* **428**, 693 (1994). doi:10.1086/174279

33. N. C. Deb, A. Hibbert, Radiative transition rates for the forbidden lines in Fe II. *Astron. Astrophys.* **536**, A74 (2011). doi:10.1051/0004-6361/201118059

34. J. C. Weingartner, B. T. Draine, Dust grain–size distributions and extinction in the milky way, large magellanic cloud, and small magellanic cloud. *Astrophys. J.* **548**, 296–309 (2001). doi:10.1086/318651

35. S. L. Lumsden, P. J. Puxley, Near-infrared spectroscopy of the ultracompact H II region1 G45.12 + 0.13. *Mon. Not. R. Astron. Soc.* **281**, 493–508 (1996). doi:10.1093/mnras/281.2.493

36. A. K. Pradhan, S. N. Nahar, *Atomic Astrophysics and Spectroscopy* (Cambridge Univ. Press, New York, 2011).

37. B.-C. Koo, arXiv:1304.3882 (2013)

38. B. T. Draine, *Physics of the Interstellar and Intergalactic Medium* (Princeton Univ. Press, NJ, 2011).

39. S. S. Tayal, Electron impact excitation collision strengths and rates for PII. *Astrophys. J. Suppl. Ser.* **150**, 465–477 (2004). doi:10.1086/380784

40. C. A. Ramsbottom, C. E. Hudson, P. H. Norrington, M. P. Scott, Electron-impact excitation of Fe II. *Astron. Astrophys.* **475**, 765–769 (2007). doi:10.1051/0004-6361:20078640

41. H. Itoh, *Publ. Astron. Soc. Jpn.* **33**, 121 (1981).

42. H. Itoh, *Publ. Astron. Soc. Jpn.* **33**, 521 (1981).

43. M. A. Dopita, L. Binette, I. R. Tuohy, Radiative shock wave theory. III. The nature of the optical emission in young supernova remnants. *Astrophys. J.* **282**, 142 (1984). doi:10.1086/162185

44. R. S. Sutherland, M. A. Dopita, Young oxygen-rich supernova remnants. 2: An oxygen-rich emission mechanism. *Astrophys. J.* **439**, 381 (1995). doi:10.1086/175181

45. W. P. Blair, J. A. Morse, J. C. Raymond, R. P. Kirshner, J. P. Hughes, M. A. Dopita, R. S. Sutherland, K. S. Long, P. F. Winkler, Hubble Space Telescope observations of oxygen-rich supernova remnants in the Magellanic Clouds. II. Elemental abundances in N132D and 1E 0102.2−7219. *Astrophys. J.* **537**, 667–689 (2000). doi:10.1086/309077

46. D. Docenko, R. A. Sunyaev, Fine-structure infrared lines from the Cassiopeia A knots. *Astron. Astrophys.* **509**, A59 (2010). doi:10.1051/0004-6361/200810366

47. J. C. Raymond, Shock waves in the interstellar medium. *Astrophys. J.* **39**, (Suppl.), 1 (1979). doi:10.1086/190562

48. D. P. Cox, J. C. Raymond, Preionization-dependent families of radiative shock waves. *Astrophys. J.* **298**, 651 (1985). doi:10.1086/163649

49. C. Mendoza, C. J. Zeippen, *Mon. Not. R. Astron. Soc.* **199**, 1025 (1982).